ELSEVIER

Chemical Engineering Science 59 (2004) 2419–2432

Chemical Engineering Science

www.elsevier.com/locate/ces

Assessment of large eddy and RANS stirred tank simulations by means of LDA

H. Hartmann[a,*], J.J. Derksen[a], C. Montavon[b], J. Pearson[b], I.S. Hamill[b], H.E.A. van den Akker[a]

[a] *Kramers Laboratorium voor Fysische Technologie, Delft University of Technology, Prins Bernhardlaan 6, 2628 BW Delft, The Netherlands*
[b] *ANSYS, The Gemini Building, Fermi Avenue, Didcot OX11 0QR, Oxfordshire, UK*

Received 15 November 2002; received in revised form 9 September 2003; accepted 8 January 2004

Abstract

Large eddy simulations (LES) and Reynolds-averaged Navier–Stokes (RANS) calculations were performed on the flow in a baffled stirred tank, driven by a Rushton turbine at $Re = 7300$. The LES methodology provides detailed flow information as velocity fluctuations are resolved down to the scale of the numerical grid. The Smagorinsky and Voke subgrid-scale models used in the LES were embedded in a numerical lattice-Boltzmann scheme for discretizing the Navier–Stokes equations, and an adaptive force-field technique was used for modeling the geometry. The uniform, cubic computational grid had a size of 240^3 grid nodes. The RANS calculations were performed using the computational fluid dynamics code CFX 5.5.1. A transient sliding mesh procedure was applied in combination with the shear-stress-transport (SST) turbulence closure model. The mesh used for the RANS calculation consisted of 241464 nodes and 228096 elements (hexahedrons). Phase-averaged and phase-resolved flow field data, as well as turbulence characteristics, based on the LES and RANS results, are compared both mutually and with a single set of experimental data.

Keywords: Stirred tank; Mixing; Turbulence; Fluid dynamics; Simulations; LDA

1. Introduction

The flow structures in a turbulently stirred tank are highly three-dimensional and complex with vortical structures and high turbulence levels in the vicinity of the impeller. Under action of a revolving impeller, the fluid is circulated through the tank. Mixing is enhanced by baffles along the tank wall preventing a solid-body rotation of the fluid.

As stirred tanks have always played an important role in industry, the understanding of the flow phenomena encountered in such tanks have been subject of research studies. These often document power number—Reynolds number relationships, and circulation times, characterizing the global flow field. Also integral investigations for selected stirrer/vessel combinations were used to derive scaling rules. In modern chemical engineering, however, there is an increasing demand for *local* flow information. For instance, yield prediction of chemically reacting fluids for a specific reactor is difficult, since most industrial flows are highly turbulent, inhomogeneous, time dependent, and cover a wide range of spatial and temporal scales (Van Vliet et al., 2001). In other applications, mixing at the small scales is important since rate-limiting phenomena take place at these scales. For example, droplet breakup is controlled by the dissipation rate of turbulent kinetic energy at the scale of the drop size, and the sizes of the turbulent eddies at this scale (Tsouris and Tavlarides, 1994; Luo and Svendsen, 1996).

Many investigations to date have been concerned with the flow in tanks stirred by a Rushton impeller as they are used for a wide range of industrial processes. This impeller induces a strong radial discharge stream. In the wakes behind the impeller blades, three dimensional vortices are formed. The variation of the radial velocity in the impeller discharge flow due to the passage of the impeller blades was found to cause an increase of the turbulence levels (Van't Riet and Smith, 1975). This non-random part of the turbulent fluctuations is sometimes presented as 'pseudoturbulence'.

Detailed flow measurement techniques, such as laser doppler anemometry (LDA) and particle image velocimetry (PIV) (Sharp and Adrian, 2001) are suitable for the investigation of highly vortical flows, and are able to resolve large-scale as well as small-scale flow structures.

* Corresponding author. Tel.: +31-15-278-7084; fax: +31-15-278-2838.
E-mail address: h.hartmann@klft.tn.tudelft.nl (H. Hartmann).

0009-2509/$ - see front matter © 2004 Elsevier Ltd. All rights reserved.
doi:10.1016/j.ces.2004.01.065

LDA investigations have identified the formation of the trailing vortex pair behind each impeller blade and provided information about the flow periodicity in the impeller vicinity and its associated increase of the turbulence levels (e.g. Yianneskis et al., 1987; Schäfer et al., 1998). LDA has proven to be more accurate in the measurement of flow fields in stirred tank reactors than other techniques (e.g. pitot-tubes, hot-wire anemometers), since it provides flow information even in unsteady and highly turbulent flow regions as well as in the return flow areas of the tank and it operates without fluid contact. However, parameters dominating the smallest scales (energy dissipation rates, spectral information at small scales, shear rates) are hardly accessible for this technique.

Since computational resources increase year-by-year, detailed computational information about the flows at the scales relevant to mixing, chemical reactions and physical processes (e.g. bubble breakup, particle collisions) can be obtained at a fraction of the cost of the corresponding experiment. Consequently, computational modeling of the flow has become an alternative route of describing flows in stirred-tanks. One of the options is a direct numerical simulation (DNS), which resolves all turbulent length and time scales by directly integrating the Navier–Stokes equations using a very fine grid. A direct simulation of stirred tank flow at industrially relevant Reynolds numbers ($Re \geqslant 10^4$) is not feasible, as the resolution of all length and time scales in the flow would require enormous amounts of grid cells and time steps. Even at the lower limit of the turbulent regime ($Re = 7300$) considered here, a true DNS would require very fine grids in the critical flow regions (such as the impeller swept volume) in order to fully resolve the flow. Bartels et al. (2001) have attempted a DNS for the same model system operating at $Re = 7300$ using a clicking/sliding mesh technique for the coupling of the rotating and fixed frame of reference. They assumed twofold periodicity of the solution domain, to keep the computational cost at an acceptable level, and the finite thickness of the blades and disk was not taken into account.

We have used the technique of large eddy simulation (LES). In LES, the Navier–Stokes equations are low-pass filtered. This way, the range of the resolved scales is reduced by the numerical grid, and the effect of the unresolved subgrid scales on the resolved large scales is taken into account with a subgrid-scale model. It has been proven to be a powerful tool to study stirred-tank flows (Eggels, 1996), as it accounts for its unsteady and periodic behavior and it can effectively be employed to explicitly resolve the phenomena directly related to the unsteady boundaries (the impeller blades). The LES methodology embedded in the lattice-Boltzmann solver has been successfully applied to single phase flow phenomena (macro-instabilities in a stirred tank by Hartmann et al. (2004)) as well as multiphase systems (solids suspension in a stirred tank by Derksen (2003)). With LES, the computational effort is high but smaller than that of a DNS.

Most of the computational fluid dynamics (CFD) simulations solve the Reynolds-averaged Navier–Stokes (RANS) equations in combination with a closure model for the Reynolds stresses. Flow periodicity and unsteadiness are taken into account with the sliding mesh procedure, in which the geometry of the individual blades is modeled using a grid rotating with the impeller, whereas the bulk flow is calculated with a stationary frame. In contrast to LES, in the RANS approach it is difficult to distinguish the part of fluctuations, that is explicitly resolved and the part represented by the Reynolds stresses. Contrary to the DNS work of Bartels et al. (2001), the full solution domain has been simulated in the present LES and RANS simulations, and the blades and disk were of finite thickness.

Nowadays, the RANS approach is commonly applied for the calculation of the complex flows in large-scale industrial reactors. As computational resources are expected to increase further in future, detailed local flow information of industrial, chemical reactors becomes within reach. As a result, the LES methodology is believed to become an engineering tool. Therefore, extensive comparisons with experimental data and RANS predictions are necessary, which was the purpose of the work presented in this paper. The flow geometry considered in this research was a Rushton turbine stirred vessel. In the LES, the standard Smagorinsky subgrid-scale model and the Voke subgrid-scale model were adopted for turbulence modeling. For the RANS calculation, the shear-stress-transport (SST) model was used. First, the behavior of the LES subgrid-scale models is checked. Subsequently, comparisons of the velocity and turbulent kinetic-energy fields are made, phase-averaged and phase-resolved (near impeller). Attention is also paid to the computed energy dissipation field and the (an)isotropy of the flow field. These latter predictions are hardly accessible experimentally, but they are of interest for many mixing applications.

2. Stirred vessel configuration

The stirred vessel reactor used in this research was a standard configuration cylindrical vessel of diameter $T = 150$ mm, with four equispaced baffles of width $0.1T$ with a small clearance of $0.017T$ and a liquid column height of $H = T$, as shown in Fig. 1. A lid was positioned at height H, to prevent entrainment of air bubbles.

The working fluid was silicon oil of density 1039 kg/m^3 and dynamic viscosity 15.9 mPa s. The impeller rotational speed was 2672 rpm, resulting in a flow Reynolds number ($Re = \rho N D^2/\mu$, ρ is the fluid density, μ is the fluid dynamic viscosity and N is the impeller rotational speed in rev/s) of 7300 and a tip speed of 7 m/s.

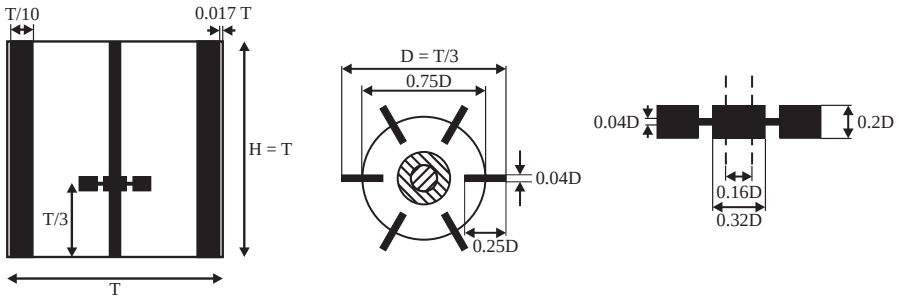

Fig. 1. Cross-section of the tank (left). Plan view (middle) and cross-section (right) of the impeller. At the top level there is a lid. The impeller is a Rushton turbine.

3. Experimental method

As a standard LDA system only supplies flow information at a single point, data acquisition was automated to enable a rapid determination of the entire flow field. A multifunctional stirrer test rig has been developed at the Institute of Fluid Mechanics (LSTM), and the entire measuring circuit was refractive index matched. The rotational speed of the impeller was measured by means of an optical shaft encoder, which was coupled to the impeller shaft. The detailed experimental results reported in this paper are taken from (Schäfer, 2001). More detailed description of the experimental setup can be found in the paper of Schäfer et al. (1997) that reports results conducted at $Re = 1200$, and the experimental procedure is described by Schäfer et al. (1998).

The vertical measurement plane was located midway between two baffles. The complete phase-averaged flow field was measured with a high resolution of 4 mm in axial and radial directions. Phase-resolved measurements in a range of 0°–60° behind the blade were made in the vicinity of the impeller stream with a resolution in axial and radial directions of 1 and 2 mm inside and outside the impeller swept volume, respectively. The measurements were performed for the axial, radial and tangential mean velocity components and their corresponding RMS levels.

4. Computational method

4.1. RANS simulation

The three dimensional simulations were performed using the computational fluid dynamics code CFX version 5.5.1, a finite-volume-based computational fluid dynamics analysis program, which solves the Navier–Stokes equations. Turbulence was modeled using the SST model (Menter, 1994), which is a combination of the k–ω model near the wall and the k–ε model away from the wall. In this way, both models are used in areas where they perform best. The reason for making use of this model was that the mesh was well resolved, resulting in y^+ values that tended to be lower than 11. By using the SST model, CFX-5 uses an automatic wall function, which blends smoothly between a low Reynolds formulation and a standard log-wall function. This gives a more accurate representation of the friction at the wall in the areas where y^+ is smaller than 11.

For the mixing vessel simulations performed, the computational mesh is made up of two parts: an inner rotating cylindrical volume enclosing the impeller, and an outer, stationary, annular volume containing the rest of the vessel. The sliding mesh procedure was applied, which is in fact a transient method. At each time step the inner grid is rotated with a small incremental angle, and the flow field is recalculated taking into account the additional velocity due to the motion of the grid. The location of the interface between the two volumes was such that the region of flow periodicity was contained within the sliding mesh. The mesh used for the RANS simulation consists of 241,464 nodes and 228,096 elements (hexahedrons). An illustration of the computational mesh is given in Fig. 2.

In the sliding mesh procedure, the transient rotor-stator frame change model was used, which predicts the true transient interaction of the flow between a stator and rotor passage. This model forms part of the general grid interfaces (GGI), which refers to a class of grid connection technology (CFX-5, 2002). As a consequence of the sliding mesh technique, the computer resources are relatively large, in terms of simulation time, disk space and quantitative post processing of the data.

Upon simulation, a blended advection scheme for the momentum and continuity equations was used to minimize effects of false diffusion. This scheme is based on upwinding along a streamline with the addition of numerical advection correction (NAC). With a blending factor of 1, the scheme is fully second-order but not bounded. Therefore, a high-resolution scheme has been used for the turbulence model equations. This scheme is also a blend between a first-order and second-order scheme, but here the blending factor is calculated based on the solution. The high resolution scheme is always bounded, and therefore does not cause overshoots or undershoots in the solution. Hence, this scheme is suitable for variables that are always positive (like k, ε and ω) or bounded (e.g. volume fractions).

First a run was made with a relatively large time step of 1.25 ms (corresponding to 20° of impeller rotation), in order to allow the solution to reach a quasi-steady state.

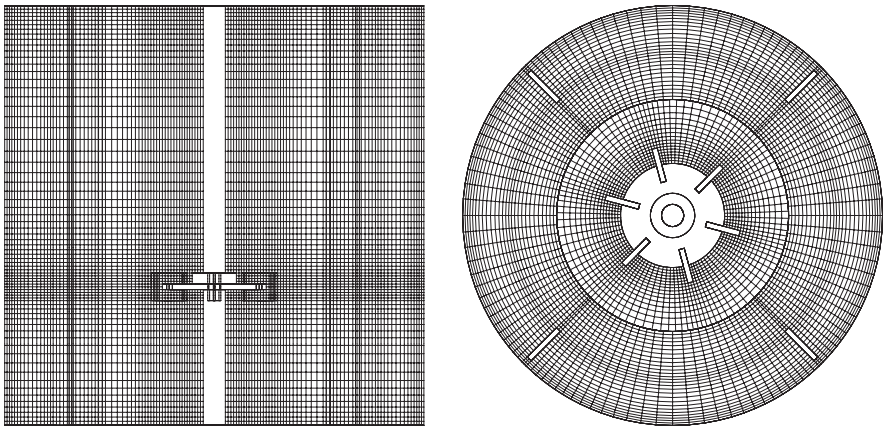

(a) (b)

Fig. 2. Vertical (a) and horizontal (b) view of the mesh in the RANS calculations.

The run has then been carried on with a smaller time step of 250 μs (i.e. 4° of impeller rotation). Per time step 10 iterations were performed. Typically within every time step, the RMS residuals at the end of the time step are three orders of magnitude smaller than at the beginning of the time step, which indicates a reasonable level of convergence. The simulation was run on Xeon dual processors (Pentium IV) machines (Dell) with 2 Gb of memory, 2 GHz clock frequency and a Linux operating system. The final run was done on six processors in parallel.

4.2. Large eddy simulation

In a LES, the small scales in the flow are assumed to be universal and isotropic (i.e. independent of the specific flow geometry). The effect the small scales have on the larger scales is modeled with a subgrid-scale model. In this research, the well-known Smagorinsky model (Smagorinsky, 1963) was used. This is an eddy-viscosity model with a subgrid-scale eddy viscosity, v_e, which is related to the local, resolved deformation rate:

$$v_e = \lambda_{\text{mix}}^2 \sqrt{S^2}, \tag{1}$$

where λ_{mix} is the mixing length of the subgrid-scale motion and S^2 is the resolved deformation rate, defined as

$$S^2 = \frac{1}{2}\left(\frac{\partial u_i}{\partial x_j} + \frac{\partial u_j}{\partial x_i}\right)^2 \tag{2}$$

with u_i the resolved ith velocity component. Note the summation convention over the repeated indices i, j. In the standard Smagorinsky model, the ratio between the mixing length and the lattice spacing, Δ, is constant, called the Smagorinsky constant (c_s). However, near the walls, the subgrid-scale stresses should vanish, which is not automatically guaranteed in the standard Smagorinsky model. In general, this is accomplished by a reduction of the length scale λ_{mix} towards the wall. In this research, the Van Driest's wall damping function (Van Driest, 1956) is used at the tank walls, which determines the mixing length as

$$\lambda_{\text{mix}} = c_s \Delta \left(1 - \mathrm{e}^{-(y^+/A^+)}\right), \tag{3}$$

where y^+ denotes the distance from the wall in viscous wall units ($y^+ = yu^\tau/v$, u_τ is the so-called friction velocity) and A^+ is a constant taken equal to 26. A value of 0.10 was adopted for c_s, which is a typical value used in LES computations of shear-driven turbulent flows (Piomelli et al., 1988).

At relatively low Reynolds numbers ($Re = 2000$–$10{,}000$) and a fine grid, as is the case in this research, the flow in quiescent regions in the tank is completely resolved. Still, the Smagorinsky model predicts a nonzero eddy viscosity in these regions (Eq. (1)). According to Voke (1996), the Smagorinsky model is valid for high v_e/v numbers, that is for high Reynolds numbers. Based on a form of the dissipation spectrum proposed by Pao (1965), a modified Smagorinsky model was introduced by Voke (1996), which is also applicable for relatively low v_e/v numbers:

$$v_{e,V} = v_e - \beta v \left(1 - \mathrm{e}^{-(v_e/\beta v)}\right) \tag{4}$$

with $\beta = \frac{2}{9}$, v_e is the Smagorinsky eddy viscosity and $v_{e,V}$ is the Voke eddy viscosity. Fig. 3 illustrates the deviation of the Voke eddy viscosity with respect to the Smagorinsky eddy viscosity. For large v_e/v numbers the Voke eddy viscosity approaches the Smagorinsky eddy viscosity and for small v_e/v numbers (i.e. more or less resolved flow) the Voke eddy viscosity is greatly reduced. For example, for $v_e/v = 10$ and $v_e/v = 1$ the eddy viscosity is reduced with 2.2% and 22%, respectively.

With a view to the flow system studied at a Reynolds number at the lower limit of the turbulent regime, we compared the performance of the Voke subgrid-scale model (because of its adequacy at 'low' Reynolds numbers) with that of the commonly used Smagorinsky model. Hence, more

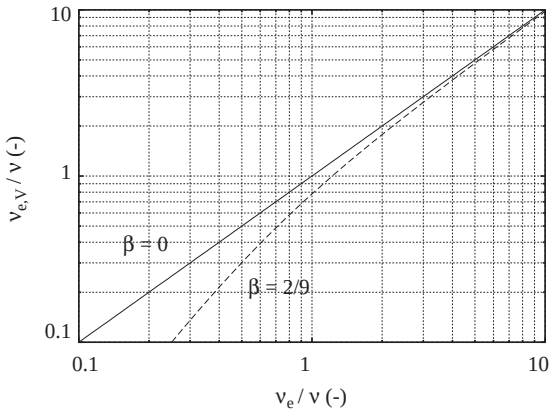

Fig. 3. The Voke subgrid-scale model, Eq. (4). While at large ν_e/ν numbers the Voke eddy viscosity (dashed line) approaches the Smagorinsky eddy viscosity (solid line), at small numbers it is significantly reduced.

advanced models like the mixed-scale models and dynamic models (see, e.g. Lesieur and Metais, 1996) have not been attempted in this work. Derksen (2001) has assessed the structure function model with the same numerical scheme as has been used here, but this model did not lead to significant changes in the results.

For the LES, a uniform, cubic computational grid of 240^3 lattice cells was defined. The diameter of the tank corresponds to 240 lattice spacings, resulting in a spatial resolution of $T/240 = 0.625$ mm. A lattice-Boltzmann numerical solver has been used for the finite-difference solution of the filtered momentum equations (Derksen and Van den Akker, 1999). This scheme is based on a microscopic model of many particles that can shuffle and collide on the numerical grid according to completely local collision rules. It can be shown that in the incompressible limit the macroscopic behavior of the particles obeys the Navier–Stokes equations (Chen and Doolen, 1998). In the current work, $N = \frac{1}{2900}$, that is, the impeller makes a full revolution in 2900 time steps (one time step equals $(2900N)^{-1} = 7.74$ μs). The diameter of the impeller equals 80 lattice spacings. As a result, the tip speed, v_{tip}, of the impeller was 0.09 (in lattice units, i.e. lattice spacings per time step), which is sufficiently low for meeting the incompressibility limit in the lattice-Boltzmann discretization scheme.

At the bottom and top of the tank a no-slip boundary condition was imposed. Inside the computational domain, the cylindrical tank wall, the baffles, the impeller, and the impeller shaft were defined by sets of points. A forcing algorithm (Derksen and Van den Akker, 1999) takes care of the no-slip boundary conditions at these points. The algorithm calculates forces acting on the flow in such a way that the flow field has prescribed velocities at points within the domain. As a geometry point does not need to coincide with the lattice nodes, interpolation (second order) of the flow velocities at the surrounding lattice sites is used to obtain the flow velocity at that point. The spacing between the geometry points has to be set such (i.e. smaller than a lattice spacing), that the fluid cannot penetrate at the surface of e.g. an impeller blade. This technique is very flexible, as there is no need for building a new computational mesh when adapting the geometry.

On every grid node 21 (18 directions for the LB particles and three force components) single-precision, real values need to be stored. The memory requirements of the simulation are proportional to the grid size, resulting in an executable that occupies $240^3 \times 21 \times 4 \approx 1.16$ GB of memory. The simulations where performed on an in-house PC cluster with Intel 500 MHz processors using a MPI message passing tool for communication. The simulations were run on four or six processors in parallel. Since the entire tank was simulated, statistical information of the flow was stored in four vertical planes midway between two baffles. Hence, four statistically independent realizations of the flow contributed to the averaging procedure. The results were averaged over 15 impeller revolutions.

5. Results

5.1. Behavior of the subgrid-scale models

Because the Reynolds number investigated in the present work is at the lower limit of the turbulent regime (Re=7300), the performance of the two subgrid-scale models applied in the LES should be checked. As a fine-grid resolution was used, the results of the LES performed might nearly resemble the results of a DNS.

Fig. 4 shows phase-averaged plots of the eddy viscosity distribution in a vertical plane midway between two baffles for both subgrid-scale models applied. The results of the eddy viscosity distribution for both subgrid-scale models clearly show that the eddy viscosity in the bulk flow is less than 10% of the kinematic viscosity. From that it can be concluded that the Kolmogorov scale in the bulk flow becomes of the order of the grid spacing, and as a consequence the results would resemble those of a DNS. However, in the impeller region and the discharge flow the eddy viscosity becomes of the order of the kinematic viscosity. Moreover, instantaneous realizations showed eddy viscosities of two to four times the kinematic viscosity. As a result, the present grid resolution would have been too coarse to capture all the turbulent scales. A DNS with the present grid resolution may therefore not accurately capture the flow phenomena occurring in the impeller region and the discharge flow where most of the mixing takes place. The authors note that for further evaluations of the subgrid-scale models, the present results should also be compared to those of a DNS with the same grid resolution. Further evaluations of the Smagorinsky model at a higher Reynolds number (i.e. $Re = 29,000$) with the same numerical scheme as is used in the present work are presented in the paper by Derksen and Van den Akker (1999).

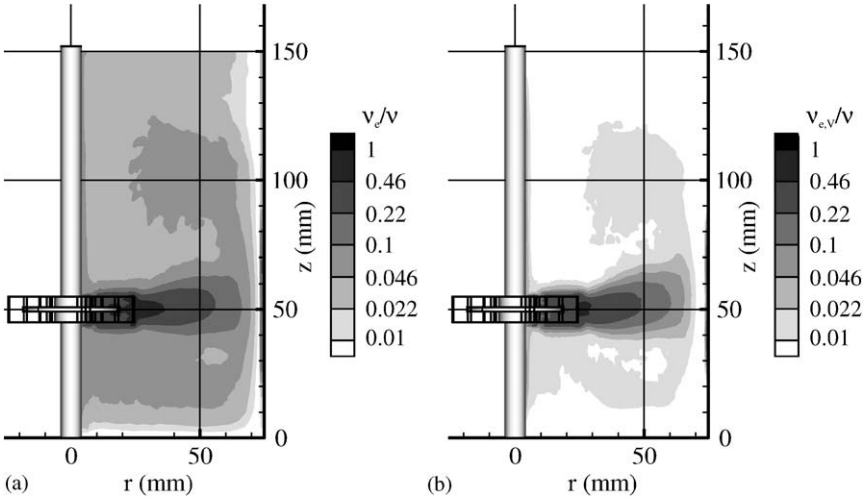

Fig. 4. Phase-averaged plot of the eddy viscosity. (a) LES: Smagorinsky model, (b) LES: Voke model.

A direct comparison between Fig. 4a and b shows a reduction of the Voke eddy viscosity with respect to the Smagorinsky eddy viscosity. The relative reduction of the eddy viscosity in the bulk flow is more pronounced than in the impeller outflow region, as expected (see Fig. 3).

5.2. Phase-averaged flow field and turbulence levels

In comparing the LES results with experimental and RANS- based data, the focus is first on the global, phase-averaged flow field. Fig. 5 shows the experimental, RANS- and LES-based results of the global, phase-averaged flow field and its associated turbulent kinetic energy levels, midway between two baffles. The dominant flow features are the large two circulation loops, one below the impeller with downward flow near the tank wall and upward flow near the axis and one above the impeller with upward flow near the tank wall and downward flow near the axis. The upper circulation loop does not extend to the top of the tank, and consequently the fluid volume in the upper part of the tank (about 14–18% of the total tank volume) is badly mixed.

The LES for both subgrid-scale models (see Fig. 5c and d), as well as the RANS simulation show good correspondence with respect to the form and center of the lower circulation loop. With respect to the upper circulation loop, a deviation of the separation point is observed between the LES and experimental results. The experimental result shows an average upward flow near the tank wall till $z/T = 0.8$, whereas the LES results with the Smagorinsky and Voke model show an upward flow till $z/T = 0.73$ and 0.7, respectively. The separation location of the upper circulation loop ($z/T = 0.8$) has been well captured by the RANS simulation, although the latter shows some spurious flow at the top of the tank. It is believed that this spurious flow is associated with the fact that the run has not fully reached its pseudo-stationary state, since it is more pronounced in the early stages of the simulation (not shown). The circulation in the lower circulation loop is stronger compared to the experimental result. We further note that the k–ε and DNS results of Bartels et al. (2001) also predict the wall separation point at a too low position ($z/T = 0.7$).

Velocity fluctuations in a turbulently stirred tank are partly periodic (directly related to the blade passage frequency) and partly random (turbulence). As a result, the kinetic energy can be divided in a random part and a coherent part. The *total* kinetic energy, k_{tot}, in the velocity fluctuations is

$$k_{\text{tot}} = k_{\text{coh}} + k_{\text{ran}} = \tfrac{1}{2}(\overline{u_i^2} - \overline{u_i}^2), \tag{5}$$

where k_{coh} and k_{ran} are the coherent and random contributions to the total turbulent kinetic energy, respectively. Note the summation convection over the repeated index i. The (time) averages are over all velocity samples, irrespective of the angular position of the impeller.

The random part of the kinetic energy can be determined if phase-resolved average data are available:

$$k_{\text{ran}} = \tfrac{1}{2}(\langle\overline{u_{i\theta}^2}\rangle - \langle\overline{u_{i\theta}}^2\rangle) \tag{6}$$

with $u_{i\theta}$ the ith resolved velocity component sample at the angular position θ. Consequently, the time averages are over the velocity samples at the angular position θ. The notation $\langle\,\rangle$ denotes averaging over all angular positions.

The kinetic energy in a LES is partly resolved and partly unresolved. The kinetic energy residing at the subgrid levels can be estimated based on isotropic, local-equilibrium mixing-length reasoning (Mason and Callen, 1986). A comparison between the grid-scale and subgrid-scale kinetic energy (instantaneous realization) in a midway baffle plane showed that about 0.1% of the kinetic energy is at the subgrid-scale level near the impeller and less in the rest of the tank (not shown), and the subgrid-scale contribution is therefore negligible. In the following results, the *resolved* kinetic energy is presented.

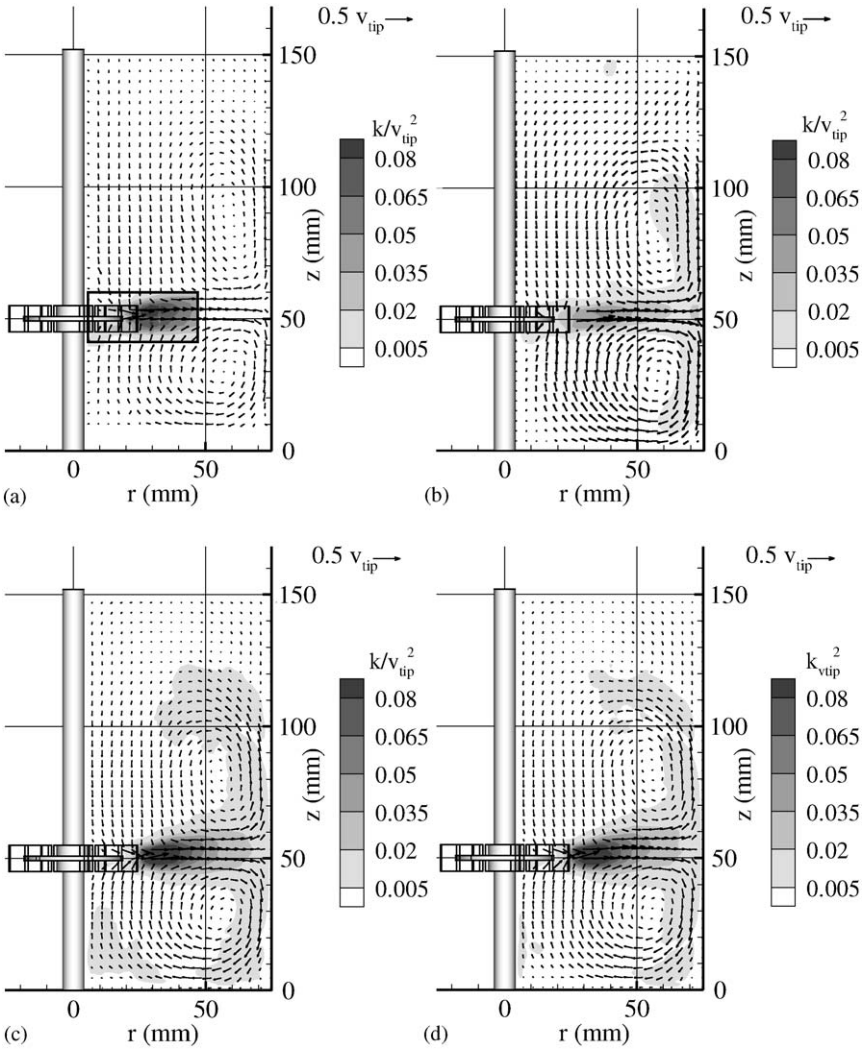

Fig. 5. Phase-averaged plot of turbulent kinetic energy (based on random velocity fluctuations) and velocity vector field. The spacing between the vectors in all subfigures is approximately the same. (a) Experiment, phase-averaged turbulent kinetic energy was only measured in the impeller region, (b) RANS, not all vectors are plotted for clarity, (c) Smagorinsky model, not all vectors are plotted for clarity, (d) Voke model, not all vectors are plotted for clarity.

The turbulent kinetic energy distributions plotted in Figs. 5 and 6 are based on the random velocity fluctuations. In case of the measurements and LES (Figs. 5a, c, d and 6a, c, d), the random part of the turbulent kinetic energy was obtained by averaging the phase-resolved experimental/numerical results, Eq. (6). In case of the transient RANS simulation (Figs. 5b and 6b), the coherent fluctuations are resolved in the transient calculations, but they are not included in the turbulent kinetic energy solved for by the RANS model. As a result, the RANS turbulent kinetic energy is regarded here to be based on random velocity fluctuations.

The results show low turbulence levels in the bulk flow. The result of the Voke subgrid-scale model shows a slight decrease in turbulent kinetic energy in the bulk flow, with respect to the result based on the Smagorinsky model (compare Figs. 5c and 5d). This observation contrasts to what is expected; a reduction of the eddy viscosity in the bulk would lead to increased levels of turbulent kinetic energy.

High turbulent kinetic energy levels are encountered in the impeller outflow region, see Fig. 6. The structure of the kinetic energy distribution of the LES calculations agrees better with the experimental results than the agreement between the RANS and experimental results.

Fig. 7 shows axial profiles of the radial and tangential velocity components and the kinetic energy based on random velocity fluctuations at three radial locations. The agreement of the radial velocity component between simulations and experiments is good, although the upward directed radial impeller outflow is more pronounced in the LES with the Voke subgrid-scale model (see Fig. 7a). All simulations overestimate the tangential velocity component at the impeller tip (i.e. $r/T = 0.183$; $z/T = 0.32$–0.35). While the agreement of the tangential velocity component for the LES

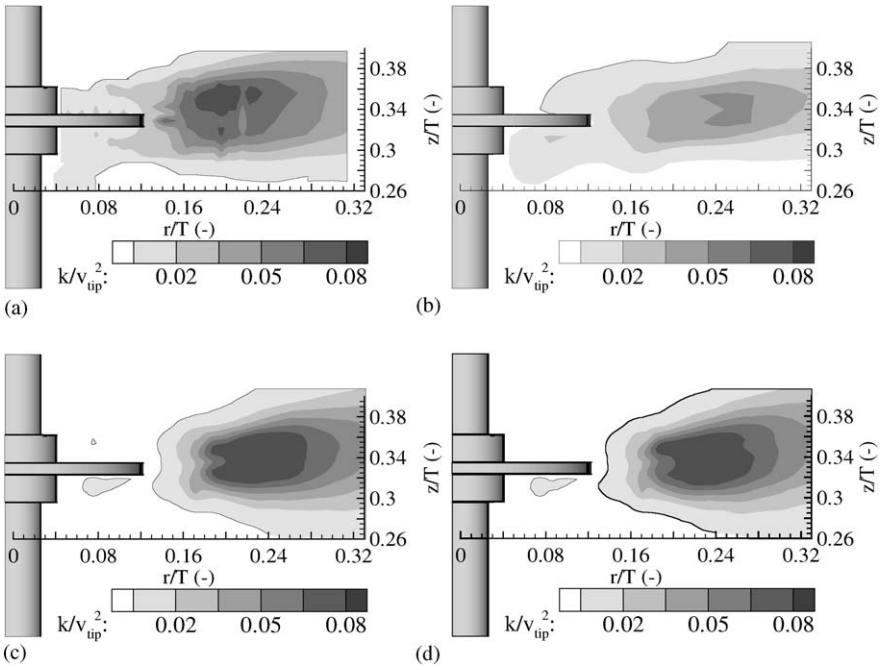

Fig. 6. Phase-averaged plot of turbulent kinetic energy (based on random velocity fluctuations in the vicinity of the impeller. (a) Experiment, (b) RANS, (c) LES: Smagorinsky model, (d) LES: Voke model.

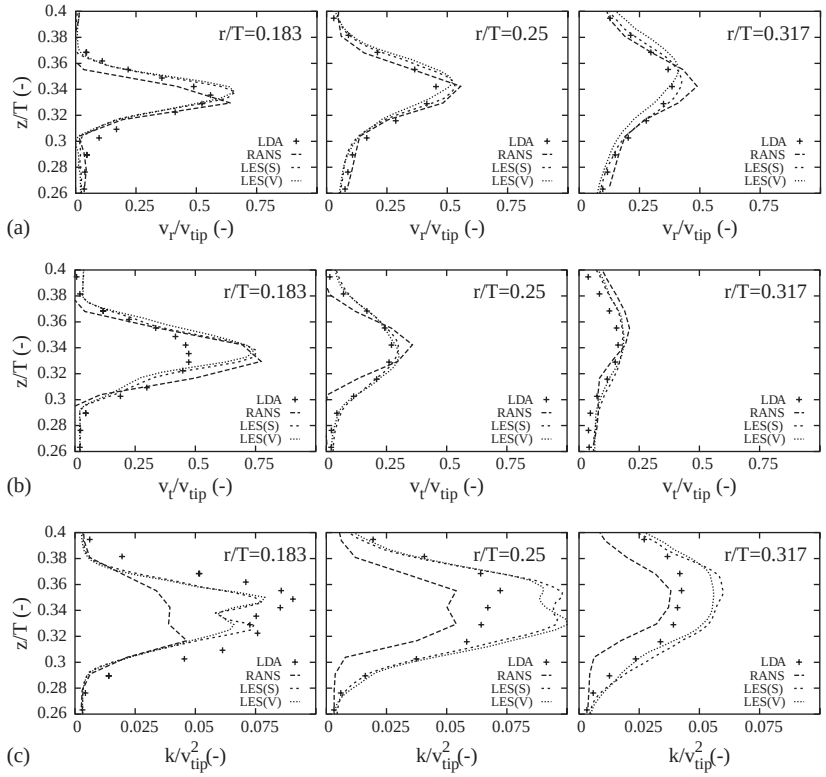

Fig. 7. Phase-averaged axial profiles of the radial (a) and tangential (b) velocity components and the kinetic energy of the random velocity fluctuations (c) at three radial locations $r/T = 0.183$(left), $r/T = 0.25$(middle) and $r/T = 0.317$(right).

is good at $r/T = 0.25$ and 0.317, the RANS predictions differ from the experimental results. At $r/T = 0.183$ the turbulent kinetic energy is underpredicted by all simulations, but the agreement of the LES predictions with experimental data is better than that for RANS. Also at $r/T = 0.25$ and 0.317 the RANS predictions significantly underpredict the

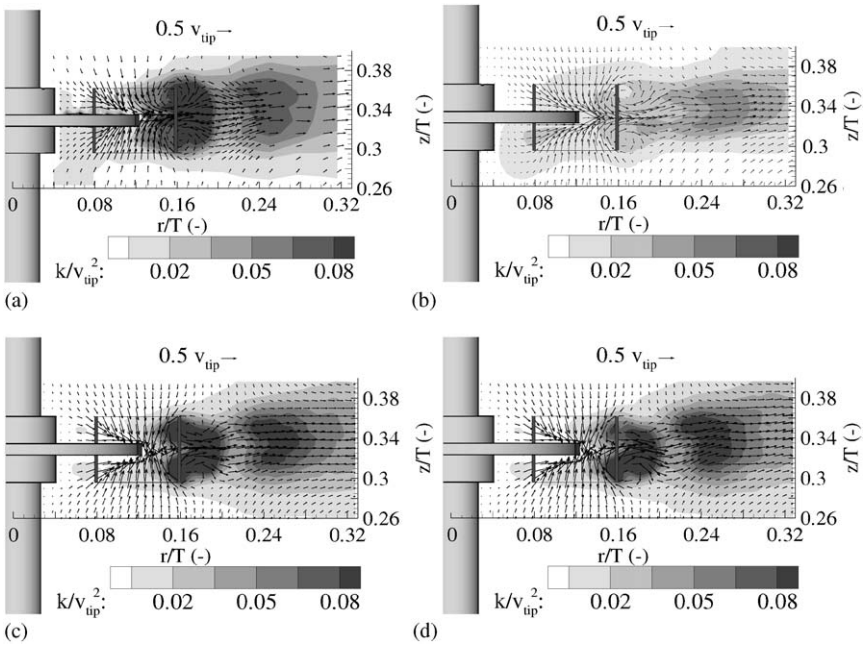

Fig. 8. Phase-resolved plot of turbulent kinetic energy (based on random velocity fluctuations) and velocity vector field at 15° behind the impeller blade. (a) Experiment, (b) RANS, (c) LES: Smagorinsky model, not all vectors are plotted for clarity, (d) LES: Voke model, not all vectors are plotted for clarity.

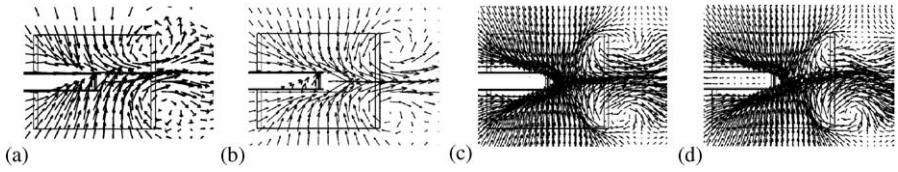

Fig. 9. Phase-resolved flow field at 15° behind the impeller blade in the domain $0.07 \leqslant r/T \leqslant 0.2$; $0.29 \leqslant z/T \leqslant 0.38$. The experimentally measured flow field is depicted in (a), and the flow field simulated by RANS, LES (Smagorinsky) and LES (Voke) in (b–d), respectively.

turbulent kinetic energy, whereas LES shows an overestimation between $z/T = 0.32$ and 0.37. However, the spreading rate (i.e. the width of the profiles) of turbulent kinetic energy predicted by LES is in accordance with the experimental data. Except for the radial velocity component, the differences between the two subgrid-scale models applied in the LES are small.

Mesh refinement and/or time-step refinement are not expected to improve substantially the predictions of the turbulent kinetic energy in the transient RANS simulation (Ng et al., 1998). It is believed that the discrepancies stem from the turbulence model employed. The SST eddy viscosity model used here assumes locally isotropic turbulence. However, if the local flow field is anisotropic (i.e. $u' \neq v' \neq w'$) the application of such a turbulence model may lead to an inaccurate prediction of the local turbulent kinetic energy.

5.3. Phase-resolved flow field and turbulence levels

In a phase-resolved experiment or simulation the position of the impeller blade, with respect to the plane where experimental and numerical results were extracted, is recorded. This allows for a reconstruction of the mean flow field and its fluctuations as function of the impeller angle.

Phase-resolved, mean flow fields in the vicinity of the impeller are shown in Figs. 8 and 10, at angles 15° and 45°, respectively. An important flow phenomenon is the trailing vortex system, that develops in the wake of the turbine blade (Fig. 8a), and is then advected by the impeller stream into the bulk of the tank. The trailing vortices are shown in more detail in Fig. 9. They die out, and the radial impeller outflow is directed slightly upward (Fig. 10a). The LES prediction with the Smagorinsky subgrid-scale model (Figs. 8c and 10c) and the RANS prediction (Figs. 8b and 10b) show a good representation of the trailing vortex system, although the upward directed radial outflow was not predicted by RANS. The Voke subgrid-scale model (Figs. 8d and 10d) predicts the lower trailing vortex as being much stronger than the upper vortex at 15°, and a remnant of that lower vortex at 45°, which does not correspond to the experimental findings.

It can be seen that the vortex structure is accompanied with high turbulent kinetic energy levels. At 15° behind the impeller blade at r/T values in between about 0.24 and 0.28

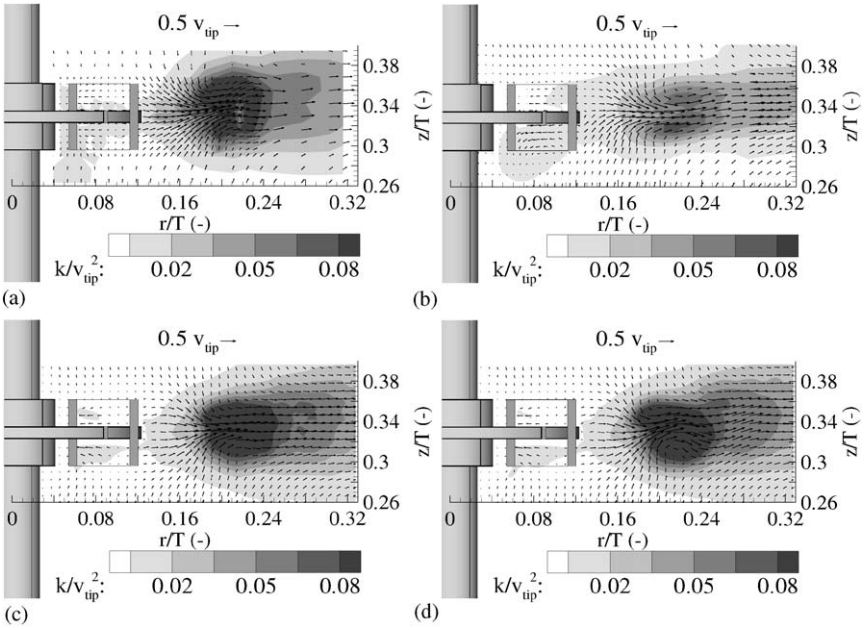

Fig. 10. Phase-resolved plot of turbulent kinetic energy (based on random velocity fluctuations) and velocity vector field at 45° behind the impeller blade. (a) Experiment, (b) RANS, (c) LES: Smagorinsky model, not all vectors are plotted for clarity, (d) LES: Voke model, not all vectors are plotted for clarity.

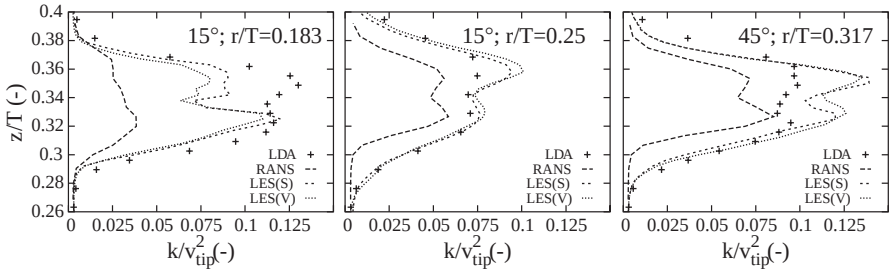

Fig. 11. Phase-resolved profiles of turbulent kinetic energy (based on random velocity fluctuations) at 15° behind the impeller blade, $r/T = 0.183$ (left) and $r/T = 0.25$ (middle), and at 45° behind the impeller blade at $r/T = 0.217$ (right).

a region is observed with high turbulent kinetic energy levels. This region of high turbulent kinetic energy is caused by the vortex system related to the previous blade passage. With the LES model, this region is slightly overpredicted. The reduction of the Smagorinsky eddy viscosity in that region by the Voke subgrid scale model is relatively small (see Fig. 4), and consequently differences of the kinetic energy between both subgrid-scale models are marginal. At 45°, the structure and levels of turbulent kinetic energy are well resolved. For the RANS calculation, the turbulent kinetic energy is mostly underestimated in areas where the trailing vortices are observed (i.e. near the tip of the blade). This underestimation may again be associated to the turbulence model used here.

Fig. 11 shows profiles of the turbulent kinetic energy at r/T=0.183, 0.25 (15° behind impeller blade) and r/T=0.217 (45° behind the impeller blade), which cover high regions of turbulent kinetic energy caused by the trailing vortices. In general, this figure shows a better agreement between LES and experimental results, compared to that between RANS and experiments. The RANS results significantly and systematically underpredict the turbulent kinetic energy. The agreement between the LES and experimental results of the width of the profiles is good, whereas Fig. 11a shows an underestimation of the turbulence levels between $z/T = 0.33$ and 0.36 and Fig. 11c shows an overestimation between $z/T = 0.32$ and 0.36.

5.4. Energy dissipation

The dissipation rate of turbulent kinetic energy (ε) is important in many mixing applications, since it controls the flow at the microscale and acts as a controlling parameter in, e.g. breakup and coalescence processes. Unfortunately, it is hardly possible to directly measure the dissipation rate. Indirect ways of measuring ε via turbulence intensities and length scales require assumptions about the nature of turbulence (e.g. isotropy or equilibrium)

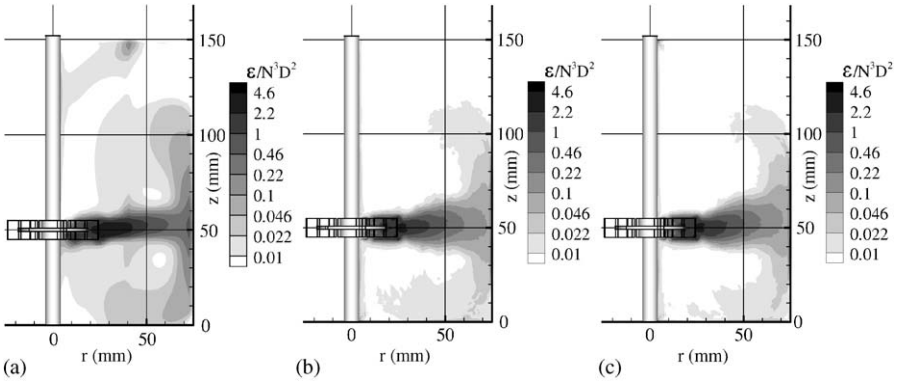

Fig. 12. Phase-averaged plot of dissipation rate of turbulent kinetic energy. (a) RANS, (b) Smagorinsky model, (c) Voke model.

which are not appropriate in stirred-tank flow. Since the predictions of the turbulent kinetic energy correspond farily well to the experimental results, it seems fair to assume that the energy dissipation rate distribution is predicted with acceptable accuracy by the simulations. By assuming local equilibrium between production and dissipation at and below subgrid-scale level, the energy dissipation rate in the LES can be coupled to the deformation rate:

$$\varepsilon = (\nu + \nu_e)S^2. \tag{7}$$

Fig. 12 shows that the dissipation rate distribution in the tank is very inhomogeneous, stressed by the log-scale used for the gray-scale coding. The energy dissipation rate in the impeller region is several orders of magnitude higher than in the bulk region.

The transient RANS result of the energy dissipation rate reveals higher energy dissipation rates compared to the LES results, and the by RANS predicited spreading rate of energy dissipation in the discharge flow is smaller than that predicted by LES. Beyond that, the structure of the distributions are similar. A region at the top of the tank and the two lobes in the impeller outflow region show increased energy dissipation rates, which are thought to be due to the fact that the run had not yet fully reached its pseudo-stationary state.

In comparing the results of the Voke model to those of the Smagorinsky model (see Figs. 12b and c), the energy dissipation rate is reduced in the bulk flow, whereas the energy dissipation rate in the impeller region is more or less unaffected. This effect is expected, since the eddy viscosity in the Voke model is more suppressed in the bulk region (more or less resolved flow) of the tank, leading to a lower energy dissipation rate in that region, see Eq. (7).

5.5. Turbulence anisotropy

The k–ε model is still widely used for simulations in stirred tank configurations, also in the present work. This model is an eddy-viscosity model and it locally assumes isotropic turbulent transport. In rotating and/or highly three-dimensional flows, the k–ε model is known to be

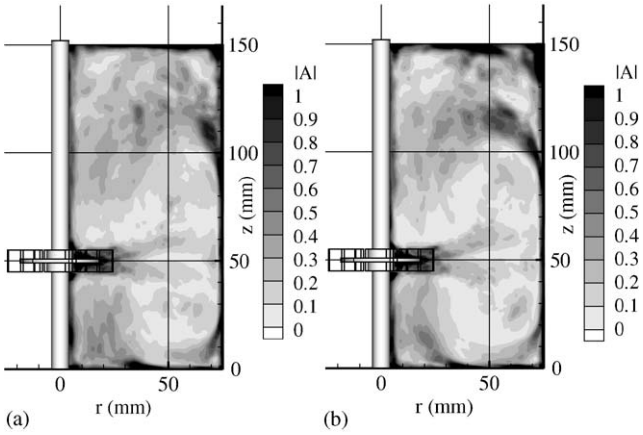

Fig. 13. Phase-averaged plot of $|A|$. (a) Smagorinsky model, (b) Voke model.

inappropriate (Wilcox, 1993). LES at least predicts the resolved part of the Reynolds stresses and thus may provide an assessment of the isotropy assumptions in the k–ε model. A treatment in terms of (an)isotropy is beneficial for a meaningful interpretation of the Reynolds stresses (Derksen et al., 1999). The Reynolds stress data will be presented in terms of the anisotropy tensor a_{ij} and its invariants. The anisotropy tensor, defined as

$$a_{ij} = \frac{\overline{u_i u_j}}{k} - \frac{2}{3}\delta_{ij} \tag{8}$$

has a first invariant equal to zero by definition. The second and third invariant respectively are $A_2 = a_{ij}a_{ji}$ and $A_3 = a_{ij}a_{jk}a_{ki}$. The range of physically allowed values of A_2 and A_3 is bounded in the (A_3, A_2) plane by the so-called Lumley triangle (Lumley, 1978). In order to characterize anisotropy with a single parameter, the distance from the isotropic state $|A| = \sqrt{A_2 + A_3}$ was defined.

Phase-averaged results of $|A|$ in a plane midway between two baffles are presented in Fig. 13. The strongest deviations from isotropy, i.e. the highest levels of $|A|$, occured in the discharge flow, the inflow regions (i.e. below and above the impeller), the boundary layers and at the separation

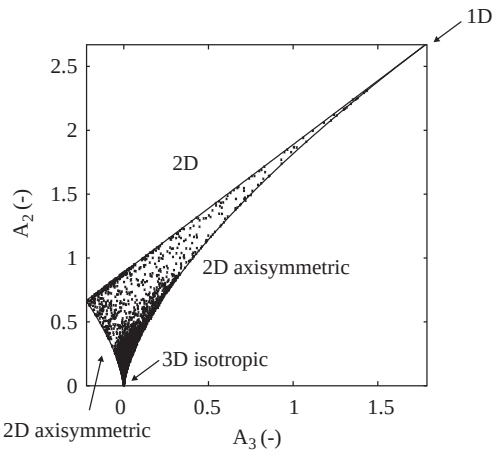

Fig. 14. The locations within the Lumley triangle of the phase-averaged points in a plane midway between two baffles. Not all points are plotted for clarity. The borders represent different types of turbulent flows: 3D isotropic turbulence, 2D axisymmetric turbulence, 2D turbulence and 1D turbulence (Lumley, 1978).

points. The turbulence anisotropy at the separation points is advected into the bulk flow. In the recirculation loops, turbulence is nearly isotropic. Fig. 14 shows the distribution of the invariants in the (A_3, A_2) plane obtained with the Smagorinsky model. The points are mostly clustered in the lower part (i.e. almost isotropic turbulence) of the so-called Lumley triangle. However, Figs. 13 and 14 both show that the assumption of locally isotropic turbulence in stirred vessel configurations is questionable. This may explain the underestimation of the turbulent kinetic energy levels in the transient RANS results observed in Sections 5.2 and 5.3.

6. Conclusions

In this paper, results of LES and RANS simulations were assessed by means of detailed LDA experiments globally throughout the tank and locally near the impeller. Two subgrid-scale models were investigated, the standard Smagorinsky model and a modified Smagorinsky model (i.e. the Voke subgrid-scale model). With a view to chemical mixing processes, the LES methodology has clear, distinct advantages over a RANS type of approach, as velocity fluctuations, and consequently the Reynolds stresses and turbulent kinetic energy, are resolved down to the scale of the numerical grid. As a result, there is a clear (spectral) distinction between the resolved and unresolved scales that is indefinite in a RANS approach.

As the experiments were conducted at the lower limit of the turbulent regime, the behavior of the subgrid-scale models applied was checked. In the bulk flow, all scales were more or less resolved, whereas in the impeller region and discharge flow the Smagorinsky and Voke eddy viscosity became of the order of the kinematic viscosity. As a result, a DNS with the LES grid resolution will not accurately capture the smallest scales in the impeller (outflow) region.

The simulated phase-averaged flow fields were in good agreement with the experimental result. The RANS flow field showed deviations in the tangential velocity component in the discharge flow (at $r/T - 0.25, 0.317$), whereas the wall separation point of the upper circulation loop in the LES flow field differed from the experimental result for both subgrid-scale models. All simulations overpredicted the tangential velocity component at the center of the impeller tip. The disagreement between the experimental and LES result of the wall separation point is thought to be due to the wall damping function used in this work. Therefore, other wall damping functions will be explored in future investigations.

The development of the trailing vortex system was well represented by the RANS simulation and LES with the Smagorinsky subgrid-scale model. The LES with the Voke subgrid-scale model showed the lower vortex as being much stronger than the upper vortex, which did not correspond to the experimental findings. The upward directed radial impeller outflow was well represented with LES, and was not found in the RANS simulation.

In general, the structure and levels of the turbulent kinetic energy in the impeller discharge flow were better represented by LES than by the RANS simulation. The levels predicted by the RANS simulation systematically and significantly underpredicted the experimentally obtained levels. The levels of turbulent kinetic energy obtained by LES were overestimated between $z/T = 0.32$ and 0.37, except for the averaged levels at $r/T = 0.183$ that showed an underestimation between $z/T = 0.26$ and 0.4. In order to improve the LES kinetic energy predictions in the impeller outflow region, either the Smagorinsky model should also be evaluated at higher Reynolds numbers (e.g. Derksen and Van den Akker, 1999), or more advanced subgrid-scale models (e.g. mixed-scale model, dynamic Smagorinsky model, see Lesieur and Metais (1996)) might be attempted.

The dissipation of turbulent kinetic energy is very inhomogeneously distributed throughout the tank, with high levels in the impeller outflow region and low levels in the bulk of the tank. The spreading rate of energy dissipation predicted by the RANS simulation was smaller than that by LES; this was also observed for the spreading rate of the turbulent kinetic energy (i.e. by the widths of the profiles). The levels obtained by the RANS simulation were higher than those obtained by LES.

As velocity fluctuations are resolved by the numerical grid, LES enables an estimation of the turbulence (an)isotropy throughout the tank. Nearly isotropic turbulence was observed in the circulation loops. However, in the impeller stream, the boundary layers, and at the separation points turbulence was found more anisotropic, probably caused by the local, high shear rates. Consequently, the choice for making use of an isotropic eddy viscosity turbulence model should be treated with care.

For the Reynolds number being in the lower limit of the turbulent regime, the Voke subgrid-scale model was

explored that blends smoothly between a DNS in the bulk flow and an LES in the impeller region and discharge flow. This has been illustrated by the Voke eddy viscosity distribution, that showed a more pronounced relative reduction of the Voke eddy viscosity in the bulk of the tank compared to that in the impeller region and discharge flow. Despite the potential of the Voke subgrid-scale model for application at relatively low Reynolds number flows, this work did not show significant improvements in the flow-field results.

In conclusion, a transient RANS simulation is able to provide an accurate representation of the flow field, but fails in the prediction of the turbulent kinetic energy in the impeller region and discharge flow where most of the mixing takes place. In order to have a fair comparison with phase-averaged and phase-resolved experimental data, the *transient* RANS simulation has been executed in a full flow domain. Similar to an LES, such a simulation is time consuming as well. The LES performed have shown that LES provides an accurate picture of the flow field, and reasonable data of the turbulent kinetic energy directly obtained from the resolved velocity fluctuations. As LES resolves the velocity fluctuations locally, information of the turbulence (an)isotropy in, e.g. a stirred tank geometry is now available.

Notation

a_{ij}	anisotropy tensor
$\|A\|$	distance from isotropic state
A^+	constant in Eq. (3)
A_2	second invariant of anisotropy tensor
A_3	third invariant of anisotropy tensor
c_s	Smagorinsky constant
D	impeller diameter, m
k	turbulent kinetic energy, m^2/s^2
k_{coh}	turbulent kinetic energy based on coherent velocity fluctuations, m^2/s^2
k_{ran}	turbulent kinetic energy based on random velocity fluctuations, m^2/s^2
N	speed of revolution, 1/s
r	radial coordinate, m
S^2	resolved deformation rate, $1/s^2$
T	tank diameter, m
u_i	velocity component i, m/s
$u_{i\theta}$	velocity component i linked to an angular position, m/s
u_τ	friction velocity, m/s
y	distance from wall, m
y^+	distance from wall in viscous wall units
v_r	radial velocity component, m/s
v_t	tangential velocity component, m/s
v_{tip}	impeller tip speed, m/s
z	axial coordinate, m

Greek letters

β	constant in Eq. (4)
Δ	lattice spacing
ε	energy dissipation rate, m^2/s^3
θ	angle, rad
λ_{mix}	mixing length, m
μ	dynamic viscosity, kg/ms
ν	kinematic viscosity, m^2/s
ν_e	Smagorinsky eddy viscosity, m^2/s
$\nu_{e,V}$	Voke eddy viscosity, m^2/s

Acknowledgements

The authors acknowledge financial support for the 'OPTIMUM' project provided by the Commission of the European Union under the programme 'Promoting Competitive and Sustainable Growth', Contract G1RD-CT-2000-00263.

References

Bartels, C., Breuer, M., Wechsler, K., Durst, F., 2001. Computational fluid dynamics applications on parallel-vector computers: computations of stirred vessel flows. Computers and Fluids 30 (1), 69–97.

CFX-5, 2002. User manual, solver and solver manager. ANSYS, Canonsburg, PA.

Chen, S., Doolen, G.D., 1998. Lattice-Boltzmann method for fluid flows. Annual Review of Fluid Mechanics 30, 329–364.

Derksen, J.J., 2001. Assessment of Large Eddy Simulations for agitated flows. Transactions of the Institute of Chemical Engineers 79A, 824–830.

Derksen, J.J., 2003. Numerical simulation of solids suspension in a stirred tank. A.I.Ch.E. Journal 49 (11), 2700–2714.

Derksen, J.J., Van den Akker, H.E.A., 1999. Large eddy simulations on the flow driven by a Rushton turbine. A.I.Ch.E. Journal 45 (2), 209–221.

Derksen, J.J., Doelman, S., Van den Akker, H.E.A., 1999. Three-dimensional LDA measurements in the impeller region of a turbulently stirred tank. Experiments in Fluids 27, 522–532.

Eggels, J.G.M., 1996. Direct and Large-Eddy Simulations of turbulent fluid flow using the lattice-Boltzmann scheme. International Journal of Heat and Fluid Flow 17, 307–323.

Hartmann, H., Derksen, J.J., Van den Akker, H.E.A., 2004. Macro-instabilities uncovered in a Rushton turbine stirred tank by means of LES. Submitted to: A.I.Ch.E. Journal, accepted for publication.

Lesieur, M., Metais, O., 1996. New trends in large-eddy simulations of turbulence. Annual Review of Fluid Mechanics 28, 45–82.

Lumley, J., 1978. Computational modelling of turbulent flows. Advances in Applied Mechanics 26, 123–176.

Luo, H., Svendsen, H.F., 1996. Theoretical model for drop and bubble breakup in turbulent dispersions. A.I.Ch.E. Journal 42, 1225–1233.

Mason, P.J., Callen, N.S., 1986. On the magnitude of the subgrid-scale eddy coefficient in large-eddy simulations of turbulent channel flow. Journal of Fluid Mechanics 162, 439.

Menter, F.R., 1994. Two-equation eddy-viscosity turbulence models for engineering applications. AIAA Journal 32 (8), 269–289.

Ng, K., Fentiman, N.J., Lee, K.C., Yianneskis, M., 1998. Assessment of sliding mesh CFD predictions and LDA measurements of the flow in a tank stirred by a Rushton impeller. Transactions of the Institute of Chemical Engineers 76A, 737–747.

Pao, Y.H., 1965. Structure of turbulent velocity and scalar fields at large wavenumbers. Physics of Fluids 8, 1063–1075.

Piomelli, U., Moin, P., Ferziger, J.H., 1988. Model consistency in large eddy simulation of turbulent channel flows. Physics of Fluids 31, 1884–1891.

Schäfer, M., 2001. Charakterisierung, Auslegung und Verbesserung des Makro- und Mikromischens in gerührten Behältern. Ph.D. Thesis, Technische Fakultät der Universität Erlangen-Nürnberg.

Schäfer, M., Höfken, M., Durst, F., 1997. Detailed LDV measurements for visualization of the flow field within a stirred-tank reactor equipped with a Rushton turbine. Transactions of the Institute of Chemical Engineers 75A, 729–736.

Schäfer, M., Yianneskis, M., Wächter, P., Durst, F., 1998. Trailing vortices around a 45° pitched-blade impeller. A.I.Ch.E. Journal 44 (6), 1233–1246.

Sharp, K.V., Adrian, R.J., 2001. PIV study of small-scale flow structure around a Rushton turbine. A.I.Ch.E. Journal 47 (4), 766–778.

Smagorinsky, J., 1963. General circulation experiments with the primitive equations: 1. The basic experiment. Monthly Weather Review 91, 99–164.

Tsouris, C., Tavlarides, L.L., 1994. Breakage and coalescence models for drops in turbulent dispersions. A.I.Ch.E. Journal 40 (3), 395–406.

Van Driest, E.R., 1956. On turbulent flow near a wall. Journal of the Aeronautical Sciences 23, 1007–1011.

Van't Riet, K., Smith, J.M., 1975. The trailing vortex system produced by Rushton turbine agitators. Chemical Engineering Science 30, 1093–1105.

Van Vliet, E., Derksen, J.J., Van den Akker, H.E.A., 2001. Modelling of parallel competitive reactions in isotropic homogeneous turbulence using a filtered density approach for large eddy simulations. Proceedings of PVP01, 3rd International symposium on computational technologies for fluid/thermal/chemical systems with industrial applications, July 22–26, Atlanta, Georgia, USA.

Voke, P.R., 1996. Subgrid-scale modeling at low mesh Reynolds number. Theoretical and Computational Fluid Dynamics 8, 131–143.

Wilcox, D.C., 1993. Turbulence modelling for CFD. La Canãda, CA. DCW Industries.

Yianneskis, M., Popiolek, Z., Whitelaw, J.H., 1987. An experimental study of the steady and unsteady flow characteristics of stirred reactors. Journal of Fluid Mechanics 175, 537–555.